ACS APPLIED MATERIALS & INTERFACES

Research Article

www.acsami.org

Si–Mn/Reduced Graphene Oxide Nanocomposite Anodes with Enhanced Capacity and Stability for Lithium-Ion Batteries

A Reum Park,[†] Jung Sub Kim,[§] Kwang Su Kim,[‡] Kan Zhang,[†] Juhyun Park,[∥] Jong Hyeok Park,[†,‡] Joong Kee Lee,[§] and Pil J. Yoo*[,†,‡]

[†]School of Chemical Engineering and [‡]SKKU Advanced Institute of Nanotechnology (SAINT), Sungkyunkwan University, Suwon 440-746, Republic of Korea

[§]Advanced Energy Materials Processing Laboratory, Center for Energy Convergence Research, Korea Institute of Science and Technology (KIST), Seoul 130-650, Republic of Korea

[∥]School of Chemical Engineering and Materials Science, Chung-Ang University, Seoul 156-756, Republic of Korea

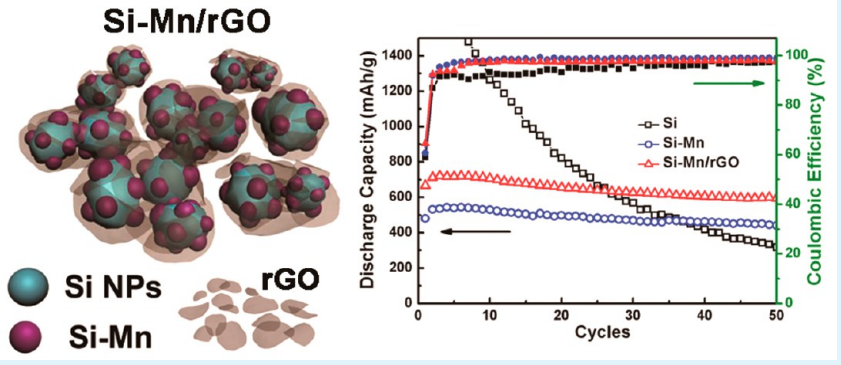

ABSTRACT: Although Si is a promising high-capacity anode material for Li-ion batteries (LIB), it suffers from capacity fading due to excessively large volumetric changes upon Li insertion. Nanocarbon materials have been used to enhance the cyclic stability of LIB anodes, but they have an inherently low specific capacity. To address these issues, we present a novel ternary nanocomposite of Si, Mn, and reduced graphene oxide (rGO) for LIB anodes, in which the Si–Mn alloy offers high capacity characteristics and embedded rGO nanosheets confer structural stability. Si–Mn/rGO ternary nanocomposites were synthesized by mechanical complexation and subsequent thermal reduction of mixtures of Si nanoparticles, MnO_2 nanorods, and rGO nanosheets. Resulting ternary nanocomposite anodes displayed a specific capacity of 600 mAh/g with ∼90% capacity retention after 50 cycles at a current density of 100 mA/g. The enhanced performance is attributed to facilitated Li-ion reactions with the MnSi alloy phase and the formation of a structurally reinforced electroconductive matrix of rGO nanosheets. The ternary nanocomposite design paradigm presented in this study can be exploited for the development of high-capacity and long-life anode materials for versatile LIB applications.

KEYWORDS: *silicon, manganese, reduced graphene oxide, lithium-ion batteries, anodes*

INTRODUCTION

The growing demand for high-performance portable electronic devices, electric vehicles, and energy integration systems has spurred efforts to develop next-generation lithium-ion batteries (LIB) with greater capacity and energy density.[1] To meet this requirement, Si is the material of choice for anode materials because of its high theoretical capacity (4200 mAh/g), which is ∼10 times greater than that of conventional graphite anodes.[2] However, Si-based anode materials suffer from large volume changes (∼300%) and the subsequent accumulation of excessive stress during lithiation–delithiation cycles, resulting in the structural collapse of the electrode and drastic capacity fading.[3] To circumvent this issue, Si alloys with a Li-inactive element, such as NiSi, MgSi, or FeSi, have been employed to minimize structural changes inside the anodes.[4−6] The alloyed transition metal species mitigates Si pulverization in response to repeated cycles and provides mechanical support for the electrochemical activity of the electrodes. However, although the cycling characteristics of Si-alloyed anodes are substantially better than those of regular Si anodes, incomplete interconnections between the alloyed domains retard cell performance; thus, capacity fading nevertheless occurs. Therefore, graphite is generally added as an electroconductive matrix to promote electrical interconnections between active materials.[7,8]

To achieve uniform integration of graphite into Si alloys, a high-temperature ball milling process is usually required.[9,10] This harsh process results in the formation of silicon oxides or other Li-inactive compounds that can undermine electrode

Received: October 18, 2013
Accepted: January 20, 2014
Published: January 20, 2014

performance. In addition, graphite may have limited capacity because of a relatively large irreversible capacity loss in the first cycle, which varies depending on the internal porosity or effective surface area.[11] For these reasons, sheetlike structured graphene has recently received much attention because of its excellent specific capacity and cyclic reversibility afforded by extra spaces for further Li-ion intercalation availability within the stacked graphene layers.[12] In addition, a very large theoretical surface area (2630 m^2/g), outstanding electrical conductivity, and mechanical rigidity of graphene make it an ideal material for imparting conductivity and structural stability to Si-based anode materials.[13−16]

Meanwhile, manganese, which is a less toxic and naturally abundant transition metal species, can be also used for LIB anode applications. Though it is Li-inactive in itself, particularly when hybridized with Si, Mn can form a Li-active Si−Mn alloy phase that is structurally stable during lithiation−delithiation cycles.[17,18] Therefore, in this study, we used Si−Mn alloy and graphene nanosheets for LIB anodes to simultaneously obtain enhanced specific capacity and cyclic stability. Si−Mn/graphene nanocomplexes were prepared by mild mechanical ball milling of Si nanoparticles, MnO_2 nanorods, and reduced graphene oxide (rGO) nanosheets, followed by thermal treatment to reduce MnO_2 (Mn^{4+}) to Mn (Mn^0). The formation of the MnSi phase within Si−Mn alloys results in a high specific capacity for electrode applications. Furthermore, uniform interdigitation of rGO nanosheets inside the MnSi alloy phase efficiently suppresses self-aggregation or electrical disconnection problems within the Li-active domains. This structural manipulation enhances the electrochemical activity of electrodes without sacrificing the structural framework, thereby resulting in enhanced cyclic stability.

EXPERIMENTAL SECTION

Synthesis of Manganese Oxide Nanorods. MnO_2 nanorods were synthesized via a quick precipitation procedure.[19] Manganese(II) chloride tetrahydrate ($MnCl_2{\cdot}4H_2O$) (0.27 g, Aldrich) was dispersed in isopropyl alcohol (50 mL, Samchun Chemical) in a round-bottomed flask equipped with a reflux condenser. The solution was heated to 83 °C while being vigorously stirred, and $KMnO_4$ (0.15 g, Samchun Chemical) dissolved in 5 mL of deionized (DI) water was then added rapidly to the boiling solution described above. Immediately thereafter, a large amount of black precipitate was produced. After being refluxed for 0.5 h, the mixture was allowed to cool to room temperature. After the precipitate had been washed with DI water and ethanol several times, followed by drying at 60 °C, MnO_2 nanorods were finally obtained.

Synthesis of Graphene Oxide (GO) and Reduced Graphene Oxide (rGO). Graphene oxide (GO) was synthesized from graphite powder (<20 μm, synthetic, Aldrich) using the modified Hummers method.[20,21] First, 0.5 g of graphite flakes and 0.5 g of $NaNO_3$ (99.0%, Yakuri Pure Chemicals) were stirred into 24 mL of H_2SO_4 (95.0%, Samchun Chemical). Then, 3 g of $KMnO_4$ (99.3%, Samchun Chemical) was added slowly while the temperature of the suspension was kept below 20 °C in ice bath. After the mixture had been stirred continuously for 1 h at 35 °C, 40 mL of DI water was slowly added to dilute the mixture and the temperature was increased to 90 °C. To reduce the residual permanganate and manganese dioxide to colorless soluble manganese sulfate, 5 mL of H_2O_2 (34.5%, Samchun Chemical) was added and the suspension was filtered with 2 L of DI water. The obtained yellow-brown suspension was exfoliated to produce single-layer graphite oxide using ultrasonication, and the unexfoliated precipitation was removed by centrifugation. The resulting aqueous suspension was completely dried at 60 °C, followed by thermal reduction in a tube furnace at 800 °C for 1 h under a H_2/Ar (1:3) atmosphere, yielding a powder of rGO nanosheets.

Preparation of Si−Mn/rGO Ternary Nanocomposites. Si−Mn nanocomposites were prepared by mechanical ball milling of Si nanoparticles (<100 nm, Aldrich) and MnO_2 nanorods at a mass ratio of 1:1. Ball milling was performed in a planetary ball milling machine (8000D Dual Mixer/Mill, SPEX SamplePrep) for the relatively short time of 30 min. To prepare ternary nanocomposites, the prepared rGO was added to the Si−Mn nanocomposites (80:20 Si−Mn:rGO in weight percent), and the mixture was ball milled for 20 min. The resulting ternary composite was annealed at 800 °C for 3 h under an Ar atmosphere to reduce MnO_2. For a comparison, the Si−Mn binary composite without rGO was also prepared by ball milling and a subsequent thermal annealing process.

Structural Characterization. Morphologies of Si−Mn and Si−Mn/rGO nanocomposite particles were characterized by field-emission scanning electron microscopy (FESEM) (JSM-7600F, JEOL) and high-resolution transmission electron microscopy (HRTEM) (JEM-3010, JEOL). Powder X-ray diffraction (XRD) patterns were obtained (D8 Focus, Bruker AXS) with Cu Kα radiation (λ = 1.5406 Å) in the 2θ range from 3° to 80° with a step size of 0.02° s^{-1}. Raman spectra were recorded using a micro-Raman spectrometer system (ALPHA 300M, WITec).

Characterization of Electrochemical Properties. Electrochemical experiments were performed using CR2032 coin cells. To prepare electrodes, Si−Mn/rGO ternary nanocomposites were mixed with conductive black (Super-P) and poly(acrylic acid) (PAA; M_w ~ 250000, 35 wt % in H_2O, Aldrich) in ethanol at a mass ratio of 70:15:15 into a homogeneous slurry. The mixed slurry was uniformly pasted on Cu foil to have ~1.5 mg/cm^2 of an active mass with a film thickness of 36 μm. Coin cells were then assembled with Li metal as the counter electrode and a polypropylene (PP, Celgard 2400, Celgard) film as the separator. A 1 M $LiPF_6$ solution in a 1:1:1 (v/v) mixture of ethylene carbonate (EC), ethylmethyl carbonate (EMC), and diemethyl carbonate (DMC) was used as the electrolyte. Electrochemical characteristics of the batteries were measured with a multichannel potentiostat/galvanostat (WMPG 1000, WonATech) at room temperature. Charge−discharge cycles were characterized galvanostatically in the potential range of 0.01−3.25 V (vs Li/Li^+) at current densities ranging from 100 to 2000 mA/g. Cyclic voltammetry was conducted in the potential range of 0.01−3.25 V at a scan rate of 0.1 mA/s. The structural change of ternary nanocomposites after charge−discharge cycles was observed via SEM. Coin cells were disassembled in a glovebox, and the separated electrode film was immersed in DMC for 10 min to remove the $LiPF_6$ electrolyte, followed by complete drying for SEM observation.

RESULTS AND DISCUSSION

The synthesis procedure used to produce Si−Mn/rGO ternary nanocomposites is shown schematically in Figure 1. First, Si

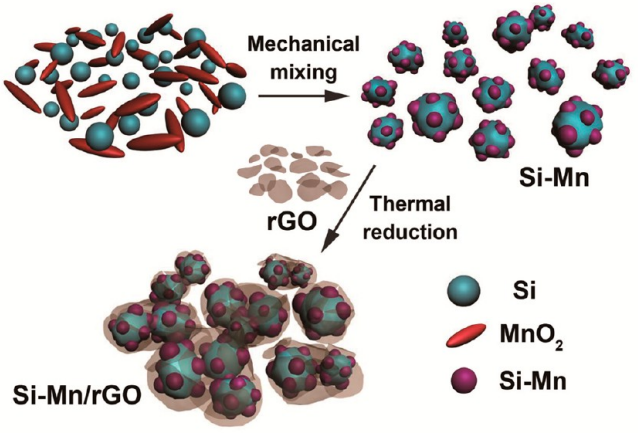

Figure 1. Schematic procedure of fabricating the Si−Mn/rGO ternary nanocomposites.

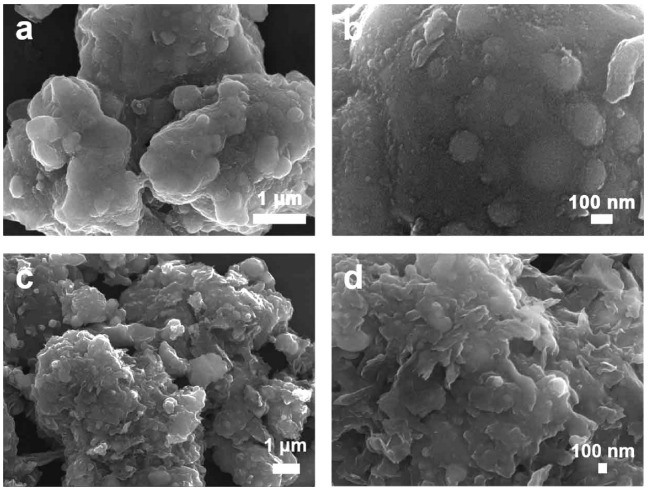

Figure 2. Comparative SEM images of (a and b) Si–Mn binary nanocomposites and (c and d) Si–Mn/rGO ternary nanocomposites.

nanoparticles (<100 nm in diameter) were mechanically mixed with MnO_2 nanorods (20–50 nm in diameter, aspect ratio of ~10) to form a homogeneously complexed phase. We used one-dimensionally structured MnO_2 nanorods to maximize interfacial contact with Si nanoparticles during complexation to suppress the self-aggregation that is frequently encountered in mixing of spherical nanoparticles.[22,23] Then, the dried rGO nanosheet powder was added to the pretreated sample followed by mixing to generate a ternary nanocomposite. Graphene oxide (GO) nanosheets were thermally reduced to form rGO prior to mixing. This procedure prevents oxidation of Si nanoparticles, moisture uptake, and subsequent gel phase formation, which are all undesirable for attaining uniform complexation.[24] Then, to reduce MnO_2 to Mn in the presence of carbon (rGO) and to promote formation of a stable MnSi alloy phase, samples were thermally annealed at 800 °C for 3 h in an Ar-purged environment (byproduct gas of CO_2 was thereby readily removed[25]). This process yielded Si–Mn/rGO ternary nanocomposites with a Li-active MnSi alloy phase encompassed by rGO nanosheets.

Morphological characteristics of Si–Mn/rGO nanocomposites were observed by scanning electron microscopy (SEM). As shown in panels a and b of Figure 2, when Si nanoparticles and MnO_2 nanorods were complexed by ball milling and thermally annealed in the absence of rGO nanosheets (Si–Mn binary nanocomposites), several micrometer-sized particles were generated, and Si–Mn alloys as a minor phase were incorporated inside the Si matrix. Because of the homogeneous mixing provided by ball milling, particles were densely agglomerated and the surface was relatively smooth. In contrast, when rGO nanosheets were added (Si–Mn/rGO ternary nanocomposites), the reduction of MnO_2 to Mn was greatly facilitated and a highly textured surface was obtained, as shown in panels c and d of Figure 2, indicating successful embedment of rGO nanosheets inside the Si–Mn alloy matrix. Here, it should be noted that an excess of Si was mixed with MnO_2 (atomic ratio of Si to Mn of ~3) to ensure full conversion of Mn species to the Si–Mn alloy phase. More importantly, this condition ensured dominant formation of the MnSi phase rather than other Li-inactive alloys.[26] Because uniform complexation of rGO nanosheets simultaneously increases the number of electrical interconnections between Li-active domains, we expected the ternary nanocomposites to show

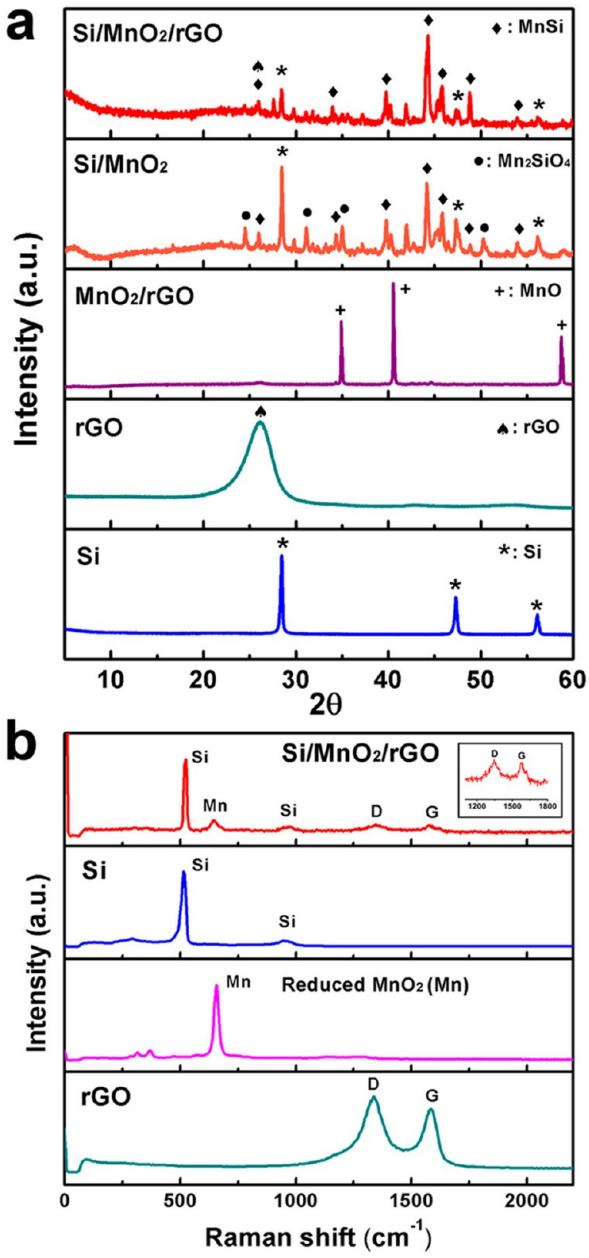

Figure 3. Crystallographic and chemical structure analysis of Si–Mn/rGO ternary nanocomposites. (a) X-ray diffractograms for Si/MnO_2/rGO, Si/MnO_2, and MnO_2/rGO complexes and for individual rGO and Si. (b) Raman spectra for the Si/MnO_2/rGO complex and for individual Si, reduced MnO_2 (Mn), and rGO.

enhanced electrochemical performance in the context of LIB anode applications.

As-prepared samples were characterized by X-ray diffraction (XRD) measurements to obtain crystallographic information (Figure 3a). For the complexation product of Si/MnO_2 (Si–Mn binary nanocomposite), peaks at 27.7°, 34.0°, 39.5°, 44.4°, and 48.9° correspond to the (110), (111), (200), (210), and (211) planes of the MnSi alloy phase, respectively, according to JCPDS 65-3297. The Si–Mn binary nanocomposite was also characterized by peaks at 28.4°, 47.6°, and 56.1° that were indexed to (111), (220), and (311) planes of Si crystals, respectively, confirming the presence of residual Si in the matrix.[27] These peaks were also clearly observed in the Si–Mn/rGO ternary nanocomposites for the complexation of Si/

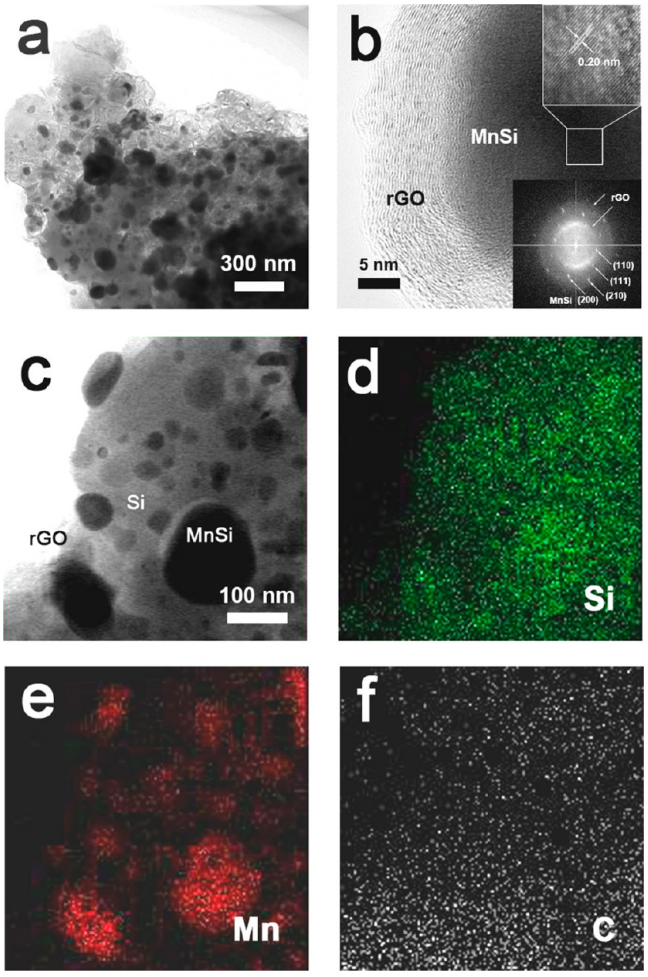

Figure 4. (a) TEM observation of the Si−Mn/rGO ternary nanocomposites. (b) HRTEM image and FFT analysis (inset). (c) TEM image of the Si−Mn/rGO ternary nanocomposites selected for EDX mappings of (d) Si, (e) Mn, and (f) C.

MnO_2/rGO, whereas the peak associated with rGO was hard to distinguish because of its less ordered status and correspondingly weaker intensity compared to other peaks. Notably, peaks associated with Mn_2SiO_4 phase formation observed in the Si−Mn binary composite almost vanished in the ternary system, indicating a role of rGO as a reducing agent. This could be more clearly confirmed by the result of complexation between rGO and MnO_2, in which the partial reduction of MnO_2 to MnO took place. These observations indicated that the rGO complexation successfully facilitated the reduction of MnO_2 in the presence of Si to form the MnSi alloy phase and, at the same time, contributed to the promotion of electrical conductivity by creating internal interconnections. In addition to these peaks, very minor peaks corresponding to Mn_5Si_3 and $Mn_{11}Si_{19}$ from Si−Mn alloy samples were also observed.[28,29] However, the peaks with the highest intensities were mostly contributed by the MnSi alloy phase. These results together with the SEM images shown in Figure 2 showed that the Si−Mn alloy consisted of microscale particulates of Si matrix and uniformly embedded nanoparticles with smaller domains of the Li-active MnSi phase.

The chemical structure of the Si−Mn/rGO nanocomposites was elucidated by analysis of Raman spectra. Consistent with the XRD results, Raman spectra for the as-prepared samples shown in Figure 3b comprised characteristic Raman peaks for individual species. Here, the spectrum for Mn was obtained from the thermally reduced MnO_2 under a H_2/Ar atmosphere. Peaks observed at 517 and 651 cm^{-1} were indexed to Si and Mn, respectively, implying the successful formation of the Si−Mn alloy.[30−32] Because Si was complexed in excess and occupied the major matrix of ternary nanocomposites, the Si peak was more pronounced than the Mn peak. In the case of rGO, both D (1350 cm^{-1}) and G (1580 cm^{-1}) bands, which are generally associated with in-plane sp^3 defects and sp^2 domains in carbon, respectively, were observed.[33] These characteristic peaks of rGO were also observed in the ternary nanocomposites, though the captured intensities were quite weak. The intensity ratio of the D band to the G band (I_D/I_G), which is used as an indicator of graphene disorder, decreased slightly from 1.08 in pure rGO to 1.00 in ternary nanocomposites, presumably indicating the enlargement of the graphitic domain during complexation with the Si−Mn phase.

To characterize the internal structure of Si−Mn/rGO ternary nanocomposites more precisely, we investigated the samples using high-resolution TEM (HRTEM). As shown in Figure 4a, the Si−Mn alloy was surrounded by multilayered rGO nanosheets, consistent with the results from SEM observations. Furthermore, the highly magnified image presented in Figure 4b revealed a lattice spacing of 0.20 nm that corresponds to the (210) plane of MnSi, verifying that the structural characteristics of the Si−Mn alloy remained intact despite rGO complexation. The inset fast Fourier transform (FFT) analysis supported the crystallographic information about MnSi in the Si−Mn/rGO ternary nanocomposites, in which (110), (111), (200), and (210) planes of MnSi were indexed. We further investigated the complexation uniformity of Si−Mn/rGO nanocomposites using energy dispersive X-ray spectroscopy (EDX). As shown in Figure 4c, black-colored domains that corresponded to the MnSi phase were randomly embedded inside the matrix of Si (expressed as the gray-colored background). The light gray-colored regions in Figure 4c indicate the outermost layer of the surrounding rGO. EDX results for Si, Mn, and C presented in panels d−f of Figure 4 demonstrated uniform incorporation of the MnSi alloy phase inside the rGO nanosheet-wrapped Si matrix.

The electrochemical performances of the Si−Mn/rGO nanocomposites as LIB anodes were tested; the results are presented in Figure 5. First, major reaction regions were investigated using cyclic voltammetry (CV) measurements as shown in Figure 5a. Presented curves were obtained from the first to tenth cycles for ternary nanocomposites in the voltage range of 0.01−3.25 V (vs Li^+/Li) at a scanning rate of 0.1 mV/s. Because current density and the level of charge transfer increased gradually during the early charge−discharge cycles, redox peaks in the first cycle were weak and occupied a broad region.[34] Cathodic peaks at 0.45 and 1.0 V indicated the formation of lithiated MnSi (Li_xMnSi). Other cathodic peaks at 0.051 and 0.20 V were assigned to the Li−Si alloying (Li_ySi) reaction. In terms of anodic reactions, delithiation of the Li_xMnSi phase as associated with a slight peak at 1.3 V was observed after the second cycle.[18] Discrete anodic peaks at 0.31 and 0.50 V corresponded to the Li−Si dealloying process.[35,36] These characteristics matched well the results from microscopic observation of SEM and TEM, wherein MnSi alloy particles were embedded inside the Si matrix. Though very minor inclusion of other Li-active alloy phases such as Mn_5Si_3 or $Mn_{11}Si_{19}$ accompanied composite formation,[37] the overall

dx.doi.org/10.1021/am404608d | ACS Appl. Mater. Interfaces 2014, 6, 1702−1708

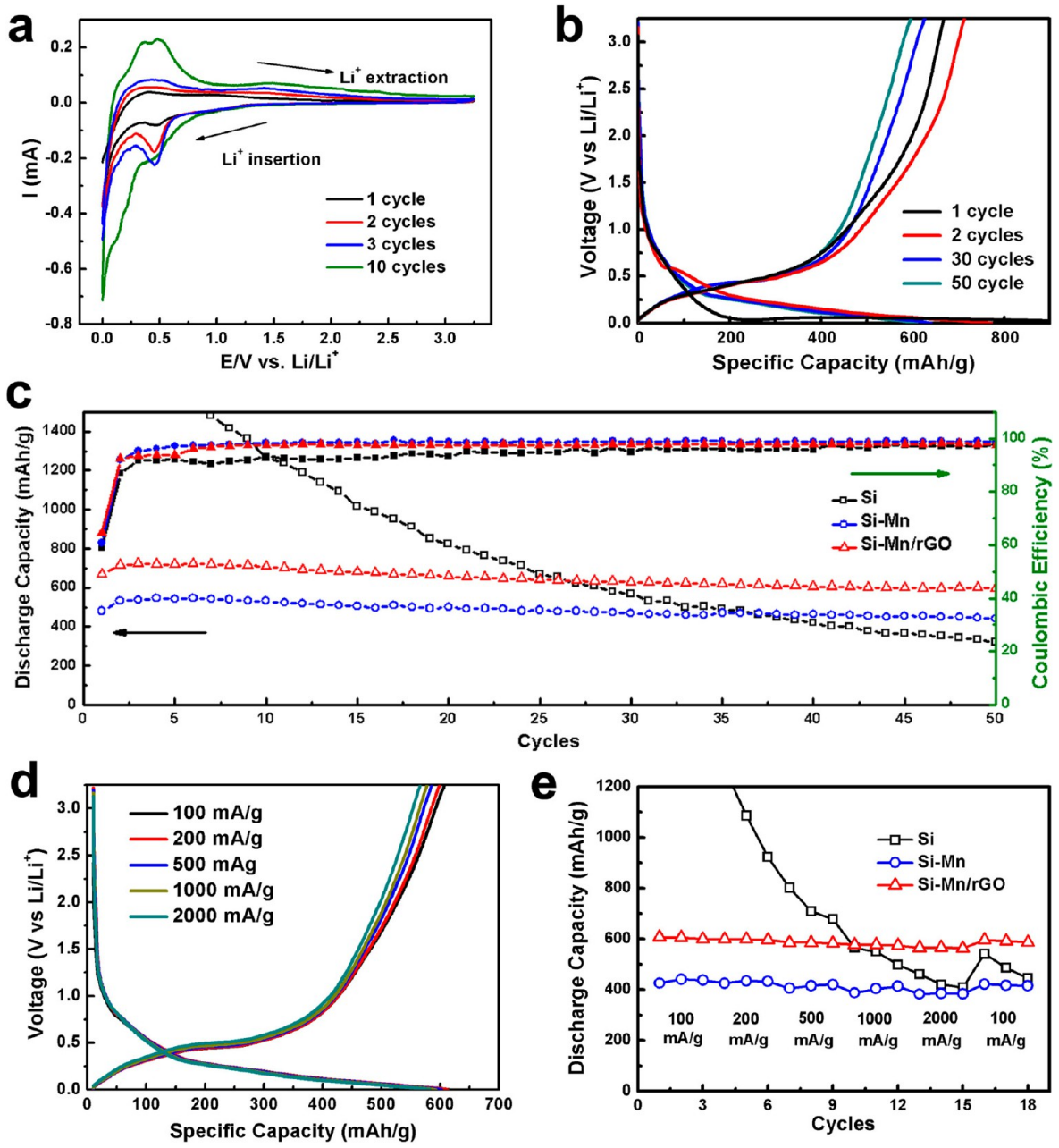

Figure 5. Electrochemical performances of Si−Mn/rGO ternary nanocomposite anodes. (a) Cyclic voltammetry. (b) Galvanostatic charge−discharge profiles in the potential range of 0.01−3.25 V (vs Li/Li^+) at a current density of 100 mA/g. (c) Capacity retention and coulombic efficiency of ternary nanocomposite electrodes during 50 cycles at 100 mA/g. (d) Galvanostatic charge−discharge profiles of the first cycle with varying current density. Voltage profiles were obtained after stabilizing the electrodes by applying 10 cycles at 100 mA/g. (e) Rate capabilities of ternary nanocomposite electrodes.

electrode performance was dominantly determined by the MnSi phase of the major species in the ternary composites.

Next, galvanostatic charge−discharge profiles were investigated as shown in Figure 5b. Capacitance−voltage measurements were performed at a current density of 100 mA/g in the active electrode within a cutoff voltage window of 0.01−3.25 V versus Li^+/Li in 1.0 M $LiPF_6$. Specific capacity values were estimated on the basis of the net weight of active materials (70 wt % of the total electrode mass). In the first charging cycle, we observed an extended slope between 0.01 and 0.1 V associated with the formation of amorphous Li_ySi. In the second cycle, a voltage plateau of 0.6 V was observed, corresponding to the lithiation reaction that forms Li_xMnSi species. Complementarily, in the discharge process, delithiation of Li_xMnSi was observed in the voltage range between 1.0 and 2.0 V.[18] In the first cycle, the charge and discharge capacity were measured as 1033 and 668 mAh/g, respectively, and the coulombic efficiency reached 64.6%. This large irreversible loss in the first cycle implied the formation of the solid electrolyte interface (SEI) between the electrode and electrolyte.[38] After 50 cycles, however, these values had stabilized to 609 and 595 mAh/g, respectively, with a coulombic efficiency of 97.6%, indicating good reversible characteristics. The obtained result was greater than previously reported values for Si/Mn/C general composites, wherein the initial discharge capacity of 463 mAh/g decreased to 387 mAh/g after 40 cycles.[26] This

dx.doi.org/10.1021/am404608d | ACS Appl. Mater. Interfaces 2014, 6, 1702−1708

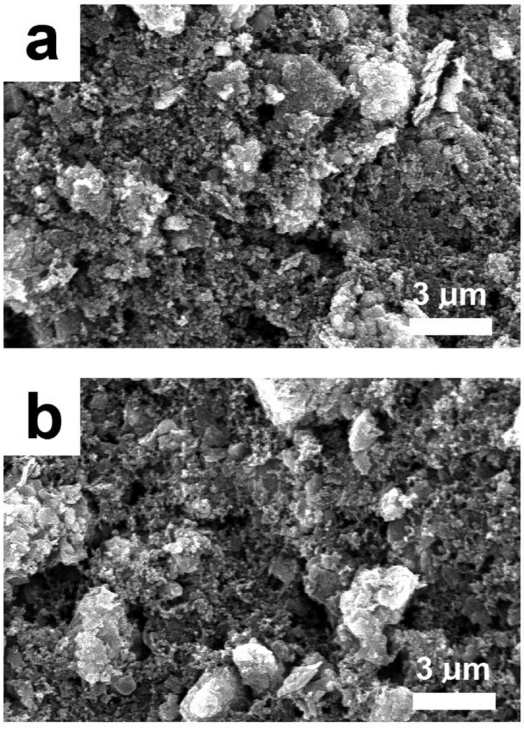

Figure 6. Comparative SEM observation of the internal structure of Si−Mn/rGO ternary nanocomposite electrodes (a) after one cycle and (b) after 30 cycles.

difference could be ascribed to a formation of the Li-active MnSi alloy phase in our ternary nanocomposites.

In addition, capacity retention of Si−Mn/rGO nanocomposites was observed to be substantially good, as shown in Figure 5c. We attributed this pronounced cyclic stability to the formation of the MnSi alloy phase and uniform embedment of electroconductive rGO nanosheets. As a result, 89.1% of the initial discharge capacity was retained after 50 cycle operations. Furthermore, the coulombic efficiency showed good reversibility (greater than ∼98 %) after ∼10 cycles. It should be noted that a slight increase in the capacity during the initial few cycles could be ascribed to the activation process of the Si matrix in the electrode. The increased intensity of redox peaks with increasing cycles as shown in CV measurements also supported this observation.[30] In addition, as revealed in Figure 5c, capacity retention characteristics of Si−Mn/rGO ternary and Si−Mn binary nanocomposites exhibited a similar trend, which indirectly proved the cyclic stability of the MnSi alloy phase. The enhanced electrical interconnection and facilitated electron transport in the ternary nanocomposites due to the rGO embedment further increased the specific capacity while preserving the cyclic stability.

The structural stability of the ternary nanocomposites was also demonstrated by the excellent rate capability characteristics shown in panels d and e of Figure 5. Here, charge−discharge cycles were measured while the current density was varied between 100 and 2000 mA/g. Notably, for the case of Si−Mn/rGO ternary nanocomposites, the discharge capacity rarely changed despite an increase in the current density, and the coulombic efficiency was consistently maintained between 97 and 98%. The structural stability of Si−Mn/rGO nanocomposites was also investigated with SEM observation for tested cells. As shown in Figure 6, internal morphologies of the electrode showed little difference between samples after one cycle and 30 cycles.

CONCLUSIONS

To summarize, we developed a novel ternary nanocomposite composed of Si, Mn, and reduced graphene oxide that showed highly enhanced performance as a Li-ion battery anode. Preferential formation of the Li-active MnSi alloy phase on the electroconductive rGO matrix ensured a high capacity because it facilitated the transport of an electron through interconnected rGOs. Furthermore, uniformly embedded electroconductive rGO nanosheets inside the ternary nanocomposites simultaneously promoted specific capacity and cyclic stability. As a result, Si−Mn/rGO ternary nanocomposites exhibited a stabilized specific capacity greater than 600 mAh/g after 50 cycles of operation while retaining ∼90% of their initial capacity. We anticipate that further structural control of ternary nanocomposites by creating an ordered structure would further enhance the electrochemical performance of these nanocomposites as high-performance anode materials for Li-ion battery applications.

AUTHOR INFORMATION

Corresponding Author

*E-mail: pjyoo@skku.edu.

Notes

The authors declare no competing financial interest.

ACKNOWLEDGMENTS

This work was supported by research grants of National Research Foundation (2012M1A2A2671795 and 2012S1A2A1A01031215), the Global Frontier R&D Program of the Center for Multiscale Energy System (2012M3A6A7055540), and the Basic Science Research Program (2012-0009158) funded by the National Research Foundation under the Ministry of Science, ICT & Future, Korea. We also acknowledge funding by the LG Yonam Foundation.

REFERENCES

(1) Tarascon, J.-M.; Armand, M. *Nature* **2001**, *414*, 359−367.
(2) Obrovac, M. N.; Christensen, L. *Electrochem. Solid-State Lett.* **2004**, *7*, A93−A96.
(3) Yang, J.; Wang, B. F.; Wang, K.; Liu, Y.; Xie, J. Y.; Wen, Z. S. *Electrochem. Solid-State Lett.* **2003**, *6*, A154−A156.
(4) Wang, G. X.; Sun, L.; Bradhurst, D. H.; Zhong, S.; Dou, S. X.; Liu, H. K. *J. Alloys Compd.* **2000**, *306*, 249−252.
(5) Roberts, G. A.; Cairns, E. J.; Reimer, J. A. *J. Electrochem. Soc.* **2004**, *151*, A493−A496.
(6) Wang, G. X.; Sun, L.; Bradhurst, D. H.; Zhong, S.; Dou, S. X.; Liu, H. K. *J. Power Sources* **2000**, *88*, 278−281.
(7) Wang, X.; Wen, Z.; Liu, Y.; Xu, X.; Lin, J. *J. Power Sources* **2009**, *189*, 121−126.
(8) Lee, H.-Y.; Lee, S.-M. *J. Power Sources* **2002**, *112*, 649−654.
(9) Lee, H.-Y.; Lee, S.-M. *Electrochem. Commun.* **2004**, *6*, 465−469.
(10) Feng, X.; Yang, J.; Gao, P.; Wang, J.; Nuli, Y. *RSC Adv.* **2012**, *2*, 5701−5706.
(11) Shim, J.; Striebel, K. A. *J. Power Sources* **2004**, *130*, 247−253.
(12) Yoo, E.; Kim, J.; Hosono, E.; Zhou, H.-s.; Kudo, T.; Honma, I. *Nano Lett.* **2008**, *8*, 2277−2282.
(13) Chou, S.-L.; Wang, J.-Z.; Choucair, M.; Liu, H.-K.; Stride, J. A.; Dou, S.-X. *Electrochem. Commun.* **2010**, *12*, 303−306.
(14) Zhou, X.; Yin, Y.-X.; Cao, A.-M.; Wan, L.-J.; Guo, Y.-G. *ACS Appl. Mater. Interfaces* **2012**, *4*, 2824−2828.

(15) Chang, J.; Huang, X.; Zhou, G.; Cui, S.; Hallac, P. B.; Jiang, J.; Hurley, P. T.; Chen, J. *Adv. Mater.* **2013**, 10.1002/adma.201302757.
(16) Wang, B.; Li, X.; Zhang, X.; Luo, B.; Jin, M.; Liang, M.; Dayeh, S. A; Picraux, S. T.; Zhi, L. *ACS Nano* **2013**, *7*, 1437−1445.
(17) Park, J. H.; Jeong, D. H.; Cha, S. M.; Sun, Y.-K.; Yoon, C. S. *J. Power Sources* **2009**, *188*, 281−285.
(18) Vediappan, K.; Lee, C. W. *J. Nanosci. Nanotechnol.* **2011**, *11*, 5969−5974.
(19) Chen, S.; Zhu, J.; Han, Q.; Zheng, Z.; Yang, Y.; Wang, X. *Cryst. Growth Des.* **2009**, *9*, 4356−4361.
(20) Park, J. S.; Cho, S. M.; Kim, W.-J.; Park, J.; Yoo, P. J. *ACS Appl. Mater. Interfaces* **2011**, *3*, 360−368.
(21) Sher Shah, Md. S. A.; Park, A. R.; Zhang, K.; Park, J. H.; Yoo, P. J. *ACS Appl. Mater. Interfaces* **2012**, *4*, 3893−3901.
(22) Wang, X.; Wen, Z.; Liu, Y. *Electrochim. Acta* **2011**, *56*, 1512−1517.
(23) Szczech, J. R.; Jin, S. *Energy Environ. Sci.* **2011**, *4*, 56−72.
(24) Xiang, H.; Zhang, K.; Ji, G.; Lee, J. Y.; Zou, C.; Chen, X.; Wu, J. *Carbon* **2011**, *49*, 1787−1796.
(25) Welham, N. J. *Int. J. Miner. Process.* **2002**, *67*, 187−198.
(26) Zuo, P.; Yin, G.; Zhao, J.; Ma, Y.; Cheng, X.; Shi, P.; Takamura, T. *Electrochim. Acta* **2006**, *52*, 1527−1531.
(27) Lee, J. K.; Smith, K. B.; Hayner, C. M.; Kung, H. H. *Chem. Commun.* **2010**, *46*, 2025−2027.
(28) Higgins, J. M.; Ding, R.; Jin, S. *Chem. Mater.* **2011**, *23*, 3848−3853.
(29) Udono, H.; Nakamori, K.; Takahashi, Y.; Ujiie, Y.; Ohsugi, I. J.; Iida, T. *J. Electron. Mater.* **2011**, *40*, 1165−1170.
(30) Bernard, M.-C.; Goff, A. H.-L.; Thi, B. V.; De Torresi, S. C. *J. Electrochem. Soc.* **1993**, *140*, 3065−3070.
(31) Buciuman, F.; Patcas, F.; Craciun, R.; Zahn, D. R. T. *Phys. Chem. Chem. Phys.* **1999**, *1*, 185−190.
(32) Tao, H.-C.; Fan, L.-Z.; Mei, Y.; Qu, X. *Electrochem. Commun.* **2011**, *13*, 1332−1335.
(33) Ferrari, A. C. *Solid State Commun.* **2007**, *143*, 47−57.
(34) Shin, H.-C.; Corno, J. A.; Gole, J. L.; Liu, M. *J. Power Sources* **2005**, *139*, 314−320.
(35) Yao, Y.; McDowell, M. T.; Ryu, I.; Wu, H.; Liu, N.; Hu, L.; Nix, W. D.; Cui, Y. *Nano Lett.* **2011**, *11*, 2949−2954.
(36) Ji, J.; Ji, H.; Zhang, L. L.; Zhao, X.; Bai, X.; Fan, X.; Zhang, F.; Ruoff, R. S. *Adv. Mater.* **2013**, *25*, 4673−4677.
(37) Anani, A.; Huggins, R. A. *J. Power Sources* **1992**, *38*, 351−362.
(38) Zhou, M.; Cai, T.; Pu, F.; Chen, H.; Wang, Z.; Zhang, H.; Guan, S. *ACS Appl. Mater. Interfaces* **2013**, *5*, 3449−3455.